Toward an Understanding of Phosphorus Cycling on Waterworlds

Cerys Holstege

Faculty adviser: Noah Planavsky

Second reader: Ruth Blake

PI: Drew Syverson

May 1, 2019

A Senior Thesis presented to the faculty of the Department of Geology and Geophysics, Yale University, in partial fulfillment of the Bachelor's Degree.

Abstract

Phosphorus is thought to be the ultimate limiting nutrient to primary productivity in the oceans today and throughout Earth's history (Bjerrum & Canfield, 2002; Laakso & Schrag, 2018; C. T. Reinhard et al., 2017). Thus, it is likely that exoplanetary biospheres are also limited by phosphorus bioavailability (Lingam & Loeb, 2019). In Earth's modern oxygenated oceans, terrestrial weathering is the only major source of bioavailable phosphorus. Conversely, marine weathering and hydrothermal alteration of basaltic oceanic crust acts as a significant sink of phosphorus through adsorption onto secondary Fe^{3+}-oxide minerals (Berner, 1973; Bjerrum & Canfield, 2002; Ruttenberg & Sulak, 2011). This framework opens up the possibility that volatile rich "waterworld" exoplanets that lack terrestrial weathering would be severely limited in bioavailable phosphorus and thus be biological deserts. Moreover, it suggests severe phosphorus limitation on early Earth prior to continental emergence and terrestrial weathering. In this study, we performed a series of basaltic glass alteration experiments in both anoxic and present-day atmospheric pO_2 conditions at a range of temperatures. Our results show that in anoxic conditions, basalt alteration is a significant source of phosphorus to seawater, on the order of riverine fluxes in modern systems. These results have broad implications not only for habitability modeling of volatile rich exoplanets -- potentially rehabilitating waterworlds that have been discounted as biological deserts -- but also for our understanding of the co-evolution of the phosphorus cycle and the oxygenation of Earth's atmosphere.

1. Introduction

Phosphorus is recognized as the limiting nutrient to primary productivity in Earth's oceans on geological timescales (Tyrrell, 1999), and likely throughout Earth's history (Bjerrum & Canfield, 2002; Laakso & Schrag, 2018; C. T. Reinhard et al., 2017). It is an essential component of the genetic and metabolic machinery of all known life (Ruttenberg, 2003). The only significant source of phosphorus to the oceans today is riverine phosphorus derived from continental weathering of rocks and soils (Ruttenberg, 2003), which is also an important long-term CO_2 sink regulating global climate. The riverine flux of particulate phosphorus to the oceans is estimated at 0.59 to 0.65 x 10^{12} moles yr^{-1} , and the dissolved phosphorus flux estimated at 0.032 to 0.058 x 10^{12} moles yr^{-1} (Ruttenberg, 2003).

Submarine weathering of basaltic oceanic crust, on the other hand, is a significant sink of phosphorus in the oceans (Berner, 1973; Wheat et al., 1996). It has been estimated that the extent of phosphorus removal in ridge-axis hydrothermal systems is at least 30 percent, and more than 80 percent in ridge-flank systems (Wheat et al., 1996). This removal is driven by adsorption onto secondary Fe^{3+}-oxide minerals, which are efficient phosphorus scavengers (Berner, 1973; Ruttenberg & Sulak, 2011; Wheat et al., 1996). In the modern oceans, some 26 percent of the dissolved riverine flux may be removed by Fe^{3+}-oxides with the vast majority of this removal occurring through ridge-flank hydrothermal processes (Wheat et al., 1996). The remainder of P sourced to oceans is buried in seafloor sediments as organic phosphorus or authigenic apatite (Ruttenberg, 2003). Submarine weathering of oceanic crust in low temperature hydrothermal systems is, like terrestrial weathering, recognized as an important CO_2 sink (Coogan & Gillis, 2013).

While it is well documented that submarine basalt alteration acts as a significant sink of dissolved phosphorus in the oxygenated modern oceans, current research has failed to address how hydrothermal phosphorus cycling could differ in anoxic ocean conditions. This oversight could limit our understanding of the phosphorus cycle on early Earth, as it is estimated that the deep oceans were not permanently oxygenated until the end of the Neoproterozoic Oxygenation Event (NOE) approximately 580 million years ago (Och & Shields-Zhou, 2012). Anoxic deep oceans would be associated with limited oxidative weathering of Fe^{2+} into Fe^{3+}-oxides and thus limited phosphorus scavenging. As such, it is possible that hydrothermal alteration of oceanic crust was a source of phosphorus throughout the Precambrian. Current modelling, however,

implicitly invokes conditions under which phosphorus is effectively scavenged through adsorption onto Fe^{3+}-oxide minerals formed from the hydration and oxidation of primary silicates in submarine basalt.

Phosphorus bioavailability is a fundamental control on atmospheric pO_2 due to its role as a globally limiting nutrient to primary productivity, the primary source of oxygen to the atmosphere (Cox et al., 2018; Laakso & Schrag, 2018). Because of this, overlooking the potential impact of lower or negligible atmospheric pO_2 levels on phosphorus fluxes in ridge-axes and ridge-flanks could not only limit our grasp of the evolution of the global phosphorus cycle, but also of its coevolution with Earth's oxygenated atmosphere. Even though existing research has recognized the interdependence of phosphorus bioavailability and atmospheric oxygen levels, many proposed models for the impact of phosphorus bioavailability on Earth's early oxygenation history fail to address the possibility that dissolved phosphorus may be liberated into seawater during anoxic weathering of the oceanic crust. Cox et al., for example, suggest that long-term cooling of the mantle led an increase in the phosphorus inventory of the continental crust due to a combination of (1) the high solubility of phosphorus in basaltic melts combined with (2) the early formation of apatite during fractional crystallization (2018). The authors argue that an increased continental phosphorus inventory could have contributed to the rise of oxygen throughout the Proterozoic. Their data set, however, explicitly excludes MORBs and only considers continental weathering as a potential source of phosphorus.

Additionally, Mills et al. suggest that a decrease in seafloor spreading rates during the Proterozoic played a significant role in the rise of atmospheric oxygen at the time, due to an associated shift toward a dominance of terrestrial weathering over oceanic weathering (2014). This argument similarly neglects the contribution that oceanic weathering could have to global phosphorus fluxes, even though they also note that the deep oceans were not oxygenated until ~580 Ma, and explicitly assumes that there is no phosphorus flux associated with seafloor weathering (Mills et al., 2014). If phosphorus can, in fact, be sourced from anoxic weathering of oceanic crust, a shift toward terrestrial weathering may not be as significant as the authors suggest.

It has also been suggested that anoxic and ferruginous oceans common on early Earth (Poulton & Canfield, 2011) resulted in enhanced phosphorus scavenging throughout the Paleozoic through adsorption onto Fe^{3+}-oxide minerals formed in oxygenated surface waters

(Laakso & Schrag, 2014; C. T. Reinhard et al., 2017). It is thus necessary that we determine if deep ocean anoxic weathering of basaltic oceanic crust away from oxygenated surface oceans can be a source of phosphorus in a low pO_2 atmosphere, which were likely common throughout the Paleozoic (Och & Shields-Zhou, 2012).

If operative, this process would not only reshape our view of the evolution of the phosphorus cycle on Earth, but would also become an important component of attempts to predict planetary phosphorus cycling on habitable exoplanets. Standard definitions of exoplanet habitability put a strong emphasis on the potential for liquid water to exist at their surface (Cockell et al., 2016), an approach that is convenient in its simplicity but that has recently been criticized for overlooking other geochemical conditions thought to be necessary for the existence of "life as we know it" (Lingam & Loeb, 2018), like the availability of bio-essential nutrients such as phosphorus. One response to this criticism is has long been argued that the potential habitability of exoplanets is dependent their surface water fraction (f_w) and their surface land fraction (f_l). Indeed, it has been argued that the evolution of extraterrestrial biospheres might only be possible on worlds with a surface water fraction between 30 and 90 percent based on the assumption that a lack of terrestrial weathering would lead phosphorus limitation (Lingam & Loeb, 2019). This framework potentially renders many volatile rich exoplanets with $f_w >> f_l$ uninhabitable, which poses a major problem for exoplanet astrobiology given that recent planetary synthesis modelling has shown that these so-called "waterworlds" are likely significantly more abundant than Earth-like planets with a more balanced ratio of f_w to f_l (Simpson, 2017). This framework, however, is based on the behavior of phosphorus in modern hydrothermal systems interacting with pervasively oxygenated deep oceans.

We performed a series of basalt glass alteration experiments in both anoxic and modern atmospheric conditions in order to assess the potential of submarine basalt alteration to act as a source of phosphorus to early Earth and in extraterrestrial biospheres. Our experimental results suggest that this type of weathering can, in fact, be a significant source of bioavailable phosphorus to oceans on Earth and other planets. This finding overturns the prevailing notion that a dominance of basalt alteration over continental weathering would have inhibited the oxygenation of Earth's early ocean-atmosphere system. Moreover, it rehabilitates waterworld exoplanets by negating the assumption that the absence of terrestrial weathering necessarily correlates with severe planetary phosphorus limitation.

2. Study area

The reactant for our weathering experiments was the glass fraction of a basalt sample sourced from near the axis of the Juan de Fuca ridge. Although mid-ocean ridge basalts (MORBs) typically do not contain igneous apatite, P^{5+} substitutes for Si^{4+} in primary silicate minerals (Koritnig, 1965; Watson, 1980), and this P may be released during submarine basalt alteration. The flow of cold seawater through the upper portion (about 0 to 600 m) of permeable, young (< 1 Ma) oceanic lithosphere at and near mid-ocean spreading ridges in hydrothermal vent systems facilitates global-scale transfer of heat and chemicals between the hydrosphere and the lithosphere (Haymon et al., 1991; Staudigel, 2003). The recognition of hydrothermal vent systems as an important component of global geochemical cycling and heat transfer was the result of discrepancies between heat transfer measured at the seafloor and what was predicted by models of lithospheric cooling. These discrepancies suggested that the lithosphere must be additionally cooled by widespread hydrothermal venting (Stein & Stein, 1994). Approximately 25 percent of the Earth's lithospheric heat loss is attributable to hydrothermal venting with an estimated 80 percent of this heat loss happening in ridge-flanks at low temperatures (2 to 20 ˚C), and at most 20 percent of it attributable high temperature (about 250 to 400 ˚C) venting on the axis of spreading ridges (Wheat et al., 2017). Our basalt glass alteration experiments were conducted at low to moderate temperatures (5 to 75 ˚C) reflective of alteration in ridge-flank hydrothermal systems.

In order for low temperature venting to accommodate such a significant heat flux, large fluxes of seawater must flow through ridge-flank hydrothermal systems; the magnitude of global ridge-flank discharge is similar to global discharge of rivers to oceans (Wheat et al., 2017; Wheat & Mottl, 2000). Even minor changes to fluid chemistry in hydrothermal vent systems, then, can meaningfully impact global geochemical cycles due to the sheer magnitude of the fluid flux. Alteration of oceanic crust in hydrothermal vent systems in the modern well oxygenated ocean has been shown to change plume fluid concentrations of Rb, Mo, V, U, Mg, Phosphate, Si and Li (Wheat et al., 2017). An analysis of pore waters from the Baby Bare ridge-flank system, which is an outcrop of 3.5 Ma basement to the east of the Juan de Fuca Ridge, showed that hydrothermal reactions at low temperatures enrich fluids in Ca, Sr, Si, B, and Mn leached from the oceanic crust while simultaneously depleting hydrothermal fluids in Na, K, Li, Rb, Mg, TCO_2, alkalinity, and phosphate (Wheat & Mottl, 2000). Hydrothermal vents are also an important source of Fe^{3+}-

oxides to the oceans in plume particles as modern oxygenated oceans rapidly oxidize Fe^{2+} (Poulton & Canfield, 2011; Rouxel et al., 2016; Trocine & Trefry, 1988). It is the prevalence of Fe^{3+}-oxides that makes alteration of oceanic crust in hydrothermal vent systems a significant phosphorus sink today.

3. Methods

3.1. Citrate-bicarbonate-dithionite treatment

The reactant basaltic glass, recovered from near the axis of the Juan de Fuca Ridge, was separated from the crystalline fraction and powdered to achieve maximum reactive surface area to enhance reaction progress (average grain size 5 to 50 μm). In order to specifically remove pre-existing Fe^{3+}-oxides from the natural reactant basalt, which may have a significant effect on the mobility of PO_4^{3-} liberated from basalt upon alteration under anoxic conditions, we treated our powdered basalt glass reactant with a citrate-bicarbonate-dithionite (CBD) reductive dissolution step prior to commencement of the experiments (Mehra & Jackson, 1958). Every 4 g of basalt glass was mixed with 20 mL of 0.3 M sodium citrate ($Na_3C_6H_5O_7$) and 2.5 mL of 1 M $NaHCO_3$ and brought to 80 ˚C in a water bath. Then, 0.5 g of solid sodium dithionite ($Na_2S_2O_4$) were added and the solution was left to react for 15 minutes before filtration. The leachate solutions were analyzed using an Element inductively coupled plasma mass spectrometer (ICP-MS).

3.2. $^{29}SiO_2$ isotope spike

In a subset of both the anoxic and oxygenated basalt weathering experiments, we used an enriched dissolved $^{29}SiO_2$ tracer in our synthetic seawater solution in order to better correlate the dissolution of primary silicate minerals with PO_4^{3+} mobilization. The synthetic seawater reaction solution used in the oxygenated experiments PG-1, PG-2, and PG-3 contained 500 μmol kg^{-1} $^{29}SiO_2$. The synthetic seawater reaction solution used in the anoxic experiments AO-1 and AO-2 contained 100 μmol kg^{-1} $^{29}SiO_2$.

The enriched dissolved $^{29}SiO_2$ tracer gives the synthetic seawater an initial $^{29}Si/^{28}Si$ ratio of ~10, about 20 times higher than the natural ratio of ~0.05. The change in ^{29}Si relative to ^{28}Si was monitored over time, where it is expected that the $^{29}Si/^{28}Si$ ratio will decrease with reaction progress due to the dissolution of reactant basalt and the associated mixing of isotopically natural

SiO_2 with the enriched seawater solution. The solution is expected to eventually approach the natural ratio (~0.05) due to mass balance constraints in the experimental system.

The change in the $^{29}Si/^{28}Si$ ratio with time, $\left(\frac{^{29}Si}{^{28}Si}\right)_t$, is directly proportional to the time-dependent change in the ^{29}Si and ^{28}Si concentration in the synthetic seawater, $\frac{d^{29}Si}{dt}$ and $\frac{d^{28}Si}{dt}$, respectively, the stoichiometric coefficient and relative isotopic composition of SiO_2 representative of basalt, $v_{Si,Bslt}$, $\left(\frac{^{29}Si}{\Sigma Si}\right)_{Bslt}$ and $\left(\frac{^{28}Si}{\Sigma Si}\right)_{Bslt}$, and the surface area and dissolution rate of the basalt in the experimental system, A_{Bslt} and R_{Bslt}, respectively (Equation 1) (Zhu et al., 2016).

Equation 1: $$\left(\frac{^{29}Si}{^{28}Si}\right)_t = \frac{\frac{d^{29}Si}{dt} - v_{Si,Bslt} \cdot A_{Bslt} \cdot R_{Bslt} \cdot \left(\frac{^{29}Si}{\Sigma Si}\right)_{Bslt}}{\frac{d^{28}Si}{dt} - v_{Si,Bslt} \cdot A_{Bslt} \cdot R_{Bslt} \cdot \left(\frac{^{28}Si}{\Sigma Si}\right)_{Bslt}}$$

The use of an initial ^{29}Si spike is advantageous to merely using an increase in the total concentration of dissolved SiO_2. Unlike changes in the total concentration of dissolved SiO_2, the $^{29}Si/^{28}Si$ ratio in the solution is not affected by the formation of secondary minerals; the effects of Si isotope fractionation that occurs in secondary mineral formation has been shown to be negligible comparted to the isotope spike (Zhu et al., 2014). Moreover, the large enrichment of dissolved ^{29}Si in solution, which is about 20 times the ratio of natural abundances, allows measurement of ^{29}Si and ^{28}Si by ICP-MS to be of sufficient resolution (both ~1 to 3 percent RSD, 1σ) to monitor statistically significant changes in the solution $^{29}Si/^{28}Si$ ratio upon reaction with the natural reactant basalt.

3.3. Synthetic seawater reaction solution preparations

Our five oxygenated (PG) and four anoxic (AO) basalt alteration experiments were performed with a variety of initial synthetic seawater reaction solutions (SW-1, SW-2, SW-3, and SW-4). All synthetic seawater solutions were prepared with Milli-Q H_2O.

The first synthetic seawater reaction solution (SW-1), which was used for experiments PG-1, PG-2, and PG-3, was designed to have concentrations of dissolved components to simulate seawater but with elevated concentrations of dissolved SiO_2 due to the $^{29}SiO_2$ tracer (500 mmol kg^{-1} NaCl – 40 mmol kg^{-1} $MgCl_2$ – 20 mmol kg^{-1} $CaCl_2$ – 20 mmol kg^{-1} Na_2SO_4 – 10 mmol kg^{-1}

KCl – 500 µmol kg^{-1} $^{29}SiO_2$). For PG-3, we also added an elevated initial concentration of 50 µmol/kg of PO_4^{3-} in the form of sodium phosphate (Na_3PO_4) to the synthetic seawater solution in order to try to observe a decrease in solution ^{31}P concentration associated with adsorption of PO_4^{3-} onto secondary Fe^{3+}-oxide minerals formed over the course of the experiment (SW-2).

The third synthetic seawater reaction solution (SW-3), which was used for experiments PG-4, PG-5, AO-3, and AO-4, was also designed to have concentrations of dissolved components to simulate seawater, but was additionally enriched with $^{26}Mg^{2+}$, $^{43}Ca^{2+}$, $^{41}K^+$, and $^{88}Sr^{2+}$ (480 mmol kg^{-1} NaCl – 53 mmol kg^{-1} $^{26}MgCl_2$ – 28 mmol kg^{-1} $NaSO_4$ – 10 mmol kg^{-1} ^{41}KCl – 10 mmol kg^{-1} $^{43}CaCl_2$ – 100 µmol kg^{-1} $^{88}SrCO_3$ – 55 µmol kg^{-1} $^{6}LiCl$).

Lastly, the synthetic seawater reaction solution used in AO-1 and AO-2 (SW-4) was the same as SW-1 but with 100 µmol/kg $^{29}SiO_2$ (500 mmol/kg NaCl – 40 mmol/kg $MgCl_2$ – 16 $CaCl_2$ mmol/kg – 100 µmol/kg $^{29}SiO_2$). A summary of the synthetic seawater solution compositions is presented in Table 1, below.

Table 1: A summary of synthetic seawater reaction solution compositions.

	[a]NaCl	$MgCl_2$	$CaCl_2$	Na_2SO_4	KCl	[b]Na_3PO_4	$SrCO_3$	LiCl	$^{29}SiO_2$
SW-1	500	40	20	20	10	0	0	0	500
SW-2	500	40	20	20	10	50	0	0	500
[c]SW-3	480	53	10	28	10	0	100	55	0
SW-4	500	40	20	20	10	0	0	0	100

[a] The solution concentrations are reported in mmol kg^{-1}, except for [b]Na_3PO_4, $SrCO_3$, LiCl, and $^{29}SiO_2$ which are reported in µmol kg^{-1}. [c]In SW-3, we used $^{26}MgCl_2$, ^{41}KCl, $^{43}CaCl_2$, and $^{6}LiCl$.

3.4. Basalt alteration experiments

Two sets of long-term basalt glass–seawater alteration experiments were conducted in order to better quantify the mobility of dissolved inorganic PO_4^{3-} under a range of different dissolved O_2 concentrations: (1) five oxygenated experiments (PG-1, PG-2, PG-3, PG-4, and PG-5) with concentrations of O_2 at present atmospheric level in which we demonstrate that the liberation of PO_4^{3-} into solution is inhibited by adsorption onto Fe^{3+}-oxides associated with oxidative alteration of basalt; and (2) four anoxic experiments (AO-1, AO-2, AO-3, and AO-4) where it is expected that PO_4^{3-} adsorption will be limited due to the lack of Fe^{3+}-oxide mineral formation.

Of the oxygenated experiments, four (PG-1, PG-2, PG-3, and PG-4) were held at 5 ± 0.1 ˚C by a shaking water bath. The fifth experiment, PG-5, was held at 25 ± 0.1 ˚C. Experiments PG-1 and PG-2 were prepared with SW-1; PG-3 with SW-2; and PG-4 and PG-5 with SW-3. All of the oxygenated experiments were prepared with a water to rock ratio of 50 (4 g of basalt glass in 200 g of synthetic seawater), except for PG-1 which had a water to rock ratio of 100 (2 g of basalt glass in 200 g of synthetic seawater).

Anoxic experiments were prepared, initiated, and maintained under anoxic conditions inside a COY chamber composed of an atmosphere of 5 percent H_2 and 95 percent N_2. The synthetic seawater reaction solutions were de-oxygenated prior to initiating the experiments by 4 hours of bubbling with 100 percent N_2 gas. Two of the anoxic experiments (AO-1 and AO-3) were held at 75 ± 0.1 ˚C and two experiments (AO-2 and AO-4) were held at 50 ± 0.1 ˚C by temperature-regulated circulating oil baths inside the COY chamber. Each oil bath was wrapped in aluminum foil to shield from UV radiation, effectively preventing photo-oxidation of dissolved Fe^{2+} liberated from reactant basalt glass. Experiments AO-1 and AO-2 were prepared with SW-3, and experiments AO-3 and AO-4 were prepared with SW-4. All four anoxic experiments had a water to rock ratio of 50.

Table 2: A summary of reaction parameters for the five oxygenated and four anoxic basalt alteration experiments.

	pO_2 (PAL)	Temp. (°C)	Solution[a]	W/R ratio
PG-1	1	5	SW-1	100
PG-2	1	5	SW-1	50
PG-3	1	5	SW-2	50
PG-4	1	5	SW-3	50
PG-5	1	25	SW-3	50
AO-1	0	75	SW-4	50
AO-2	0	50	SW-2	50
AO-3	0	75	SW-4	50
AO-4	0	50	SW-2	50

[a]The synthetic seawater solution compositions of SW-1, SW-2, SW-3, and SW-4 are reported in Table 1.

All experiments were conducted in gas-tight 250 mL Pyrex reactors with two gas-tight ports, allowing for direct time-series sampling of the reactor solution without termination of the experiment and for keeping the reaction system closed to external environmental changes. Regular samples were taken over the course of between about 300 hours for the shortest running experiments (A0-3 and AO-4) and about 2600 hours for the longest running experiment (PG-3). A summary of experimental parameters for each reaction is presented in Table 2.

The time-series solution samples taken from each experiment, oxygenated and anoxic, were measured for pH immediately after sampling by use of a Ross micro-electrode, which was

calibrated with the pH buffers 4, 7, and 10 before each analysis. The error associated with the pH measurement is within ± 0.02 log units (2σ). The concentration of the dissolved components of interest and the $^{29}Si/^{28}Si$ ratio were determined with an Element inductively coupled plasma mass spectrometer (ICP-MS).

3.5. Synchrotron X-ray fluorescence mapping (SXRF)

The distribution of Fe in the reactant natural basalt was examined by synchrotron X-ray fluorescence mapping (SXRF). All of the glass basalt samples were measured in the form of polished thin sections mounted on trace-element free silica glass at the XFM beamline at the Australian Synchrotron (AS), Melbourne, Australia by Dr. Drew Syverson. The AS is a 3 GeV ring and was operated in top-up mode with a maximum current of 200 mA. The XFM beamline has a 1.9 T wiggler source and a Si(111) monochromator with an energy resolution (ΔE/E) of 1.5 x 10-4 at 10 keV. Kirkpatrick-Baez mirrors were used to focus the beam to a spot size of ~2 x 2 μm2, and each sample was measured at high resolution, oversampling with 1 μm step-size. Data were acquired in backscatter-fluorescence mode using the 386-elements Maia fluorescence detector. The SXRF data were analyzed with GeoPIXE, using the dynamic analysis (DA) method to project quantitative elemental images from the full fluorescence spectra (Fisher et al., 2015).

3.6. Scanning Electron Microscopy (SEM)

Powdered, CBD treated reactant basalt glass was imaged by a Scanning Electron Microscopy (SEM) using a JEOL JXA-8530F (FEG) “Hyperprobe” at an acceleration voltage of 10.0 kV prior to experimental alteration and following alteration in experiments PG-1 and AO-3 in order to characterize powder grains and to visualize alteration products.

4. Results

4.1. CBD leachate solution chemistry

Leachates from the CBD reductive dissolution treatment, which is specifically designed to remove pre-existing Fe^{3+}-oxides from reactant basalt glass, were concentrated in Fe. They

were also concentrated in P, as well as other components that are associated with Fe^{3+}-oxides like Mn, V, and Ni. Moreover, Al is concentrated in the leachate, which suggests that the treatment also led to the dissolution of Fe^{3+}-oxide bearing clays. CBD treatment leachate solution chemistry is reported in Table 3**.**

Table 3: CBD treatment leachate compositions

	Σ[Fe]	Σ[Mn]	Σ[PO_4]	Σ[V]	Σ[Ni]	Σ[Al]
CBD-1	80.20	1.28	1.29	0.19	0.12	66.30
CBD-2	71.21	1.17	1.05	0.17	0.11	62.05
CBD-3	71.16	1.15	1.14	0.17	0.10	65.41
CBD-4	75.05	1.20	1.30	0.18	0.11	61.10
CDB-5	68.39	1.15	1.12	0.17	0.10	55.78
CBD-6	62.23	2.13	1.25	0.17	0.16	57.51
CBD-7	64.71	1.02	1.11	0.16	0.10	53.73
CBD-8	67.08	1.05	1.25	0.17	0.11	55.59
CBD-9	66.6	1.08	1.23	0.17	0.12	55.90

The concentrations of all dissolved leachate components are reported in µmol kg^{-1}. Every 4 g of basalt glass was treated with 22.5 mL of CBD solution.

4.2. Time-series changes in solution chemistry

4.2.1. Total dissolved SiO_2

An increase in total dissolved SiO_2 is indicative of reaction progress and the dissolution of basalt during alteration. Total dissolved SiO_2 content was calculated from the sum of ^{28}Si, ^{29}Si, and ^{30}Si concentrations as measured by ICP-MS. Oxygenated experiments using reactant synthetic seawater solution enriched with a $^{29}SiO_2$ spike – PG-1, PG-2, and PG-3 – had higher initial concentrations of total dissolved SiO_2 (500 µmol kg^{-1}), and these concentrations did not increase with reaction progress. The concentration of total dissolved SiO_2 of PG-1, PG-2, and PG-3 went from 544.7 to 526.4 µmol kg^{-1}, from 517.3 to 515.9 µmol kg^{-1}, and from 520.0 to 485.2 µmol kg^{-1} at 12 hours to 612 hours, respectively. Total dissolved SiO_2, increased slightly over time oxygenated experiments with reactant synthetic seawater solution not enriched with a $^{29}SiO_2$ tracer, PG-4 and PG-5. In PG-4, the total SiO_2 in the initial sample was 8.9 µmol kg^{-1} and the final concentration was 41.8 µmol kg^{-1}. In PG-5, the concentration of dissolved SiO_2 increased from 28.9 µmol kg^{-1} to 94.6 µmol kg^{-1} (Table 4).

The higher temperature (50 and 75 ˚C) anoxic experiments saw a more marked increase in SiO_2 concentration with reaction progress. Anoxic experiments using reactant synthetic seawater solution enriched with a $^{29}SiO_2$ spike, AO-1 and AO-2, had higher initial concentrations of total dissolved SiO_2 (100 µmol kg^{-1}). Total SiO_2 concentrations for both AO-1 and AO-2 in the first sample at 12 hours are significantly higher, 664.5 µmol kg^{-1} and 378.1 µmol kg^{-1}

Table 4: Time-series solution chemistry of oxygenated basalt alteration experiments, PG-1, PG-2, PG-3, PG-4, and PG-5.

PG-1	Temp. (°C)	Time (hr)	pH_{25C}	[a]Σ[Mg]	Σ[Ca]	[b]Σ[SiO_2]	Σ[Fe]	Σ[P]	$(^{29}Si/^{28}Si)_{Aq}$
0	5	12	5.496	45.4	17.3	544.7	0.10	n.d.	0.31
1	5	60	5.536	46.2	17.2	510.1	0.41	n.d.	0.30
2	5	108	5.52	46.6	17.0	488.5	0.10	0.01	0.30
3	5	180	5.564	45.4	17.1	486.1	0.06	0.08	0.31
4	5	276	5.439	46.8	17.3	476.3	0.10	n.d.	0.31
5	5	396	5.464	46.7	17.2	502.8	[c]n.a.	n.d.	0.30
6	5	612	4.726	47.7	17.4	526.4	0.26	0.04	0.30
PG-2	Temp. (°C)	Time (hr)	pH_{25C}	[a]Σ[Mg]	Σ[Ca]	[b]Σ[SiO_2]	Σ[Fe]	Σ[P]	$(^{29}Si/^{28}Si)_{Aq}$
0	5	12	5.534	47.1	16.6	517.3	0.19	n.d.	0.30
1	5	60	5.581	45.9	16.7	511.6	0.07	0.26	0.30
2	5	108	5.484	49.4	17.3	506.0	0.10	n.d.	0.30
3	5	180	5.611	48.7	17.2	493.8	0.08	n.d.	0.30
4	5	276	5.605	51.2	17.6	525.6	0.17	0.02	0.30
5	5	396	5.602	48.7	17.1	515.7	0.08	0.06	0.30
6	5	612	5.441	48.4	16.9	515.9	0.09	0.20	0.30
PG-3	Temp. (°C)	Time (hr)	pH_{25C}	[a]Σ[Mg]	Σ[Ca]	[b]Σ[SiO_2]	Σ[Fe]	Σ[P]	$(^{29}Si/^{28}Si)_{Aq}$
0	5	12	5.423	48.5	17.1	520.0	0.18	45.05	0.30
1	5	60	5.465	49.1	17.6	557.7	0.46	45.19	0.30
2	5	108	5.459	49.2	17.8	562.4	0.10	45.55	0.30
3	5	180	5.51	48.6	17.4	537.1	0.31	45.26	0.30
4	5	276	5.523	45.5	17.5	512.3	0.37	42.39	0.30
5	5	396	5.438	44.4	17.0	511.8	0.46	42.32	0.31
6	5	612	5.411	42.6	17.0	485.2	0.14	42.08	0.32
PG-4	Temp. (°C)	Time (hr)	pH_{25C}	[a]Σ[Mg]	Σ[Ca]	[b]Σ[SiO_2]	Σ[Fe]	Σ[P]	$(^{29}Si/^{28}Si)_{Aq}$
0	5	12	6.459	69.5	9.5	8.9	0.01	0.09	0.05
1	5	60	5.681	70.6	9.5	12.2	0.06	0.27	0.05
2	5	108	5.412	71.0	9.6	17.6	0.03	0.10	0.05
3	5	156	5.411	70.8	9.6	18.0	0.17	0.71	0.05
4	5	228	5.542	69.0	9.4	21.5	0.23	0.13	0.04
5	5	324	5.655	67.3	9.1	11.7	0.05	0.54	0.04
6	5	2148	6.020	46.7	10.3	41.8	n.d.	0.12	0.05
PG-5	Temp. (°C)	Time (hr)	pH_{25C}	[a]Σ[Mg]	Σ[Ca]	[b]Σ[SiO_2]	Σ[Fe]	Σ[P]	$(^{29}Si/^{28}Si)_{Aq}$
0	25	12	5.294	72.2	9.8	28.9	0.24	0.13	0.04
1	25	60	5.624	69.3	9.2	41.7	0.22	0.21	0.04
2	25	156	5.654	69.7	9.4	27.1	1.27	0.15	0.05
3	25	1980	6.089	45.1	9.9	94.6	n.d.	0.18	0.05

[a]The major dissolved cations/anions are in units of mmol/kg. [b]The minor dissolved cations/anions are in units of µmol/kg. All of the experiments used natural reactant basalt that was treated with the CBD treatment, a reductive dissolution pretreatment to specifically remove any pre-existing Fe^{3+}-oxide minerals associated with the natural basalt recovered from the seafloor. [c]The PG-1-5 measurement for Σ[Fe] is excluded because the anomalously high value (10.08) is interpreted as sample contamination.

respectively, than that of the synthetic seawater solution. The final SiO_2 concentrations of AO-1 and AO-2 were 904.0 and 348.1 µmol kg^{-1} at 396 hours, respectively. In anoxic experiments without the additional $^{29}SiO_2$ spike, AO-3 and AO-4, the total concentration of dissolved SiO_2 also increased over time; their initial to final sample concentrations were 510.5 to 1244.2 µmol

kg^{-1} and 134.4 to 266.3 μmol kg^{-1}, respectively (Table 5; Fig. 1a). These values represent a significant increase in dissolved SiO_2 relative to the initial 0 μmol kg^{-1} concentration of SW-4.

Table 5: Time-series solution chemistry of anoxic basalt alteration experiments, AO-1, AO-2, AO-3, and AO-4.

AO-1	Temp. (°C)	Time (hr)	pH_{25C}	[a]Σ[Mg]	Σ[Ca]	[b]Σ[SiO_2]	Σ[Fe]	Σ[P]	$(^{29}Si/^{28}Si)_{Aq}$
0	75	12	5.722	53.8	28.5	664.5	n.d.	0.26	0.63
1	75	60	5.884	34.1	17.4	549.1	0.23	0.15	0.34
2	75	228	6.033	34.9	17.6	640.2	n.d.	0.46	0.21
3	75	300	6.275	43.8	23.1	873.7	0.06	0.85	0.18
4	75	396	6.148	40.7	21.5	904.0	0.46	1.18	0.14
AO-2	Temp. (°C)	Time (hr)	pH_{25C}	[a]Σ[Mg]	Σ[Ca]	[b]Σ[SiO_2]	Σ[Fe]	Σ[P]	$(^{29}Si/^{28}Si)_{Aq}$
0	75	12	5.974	49.9	26.1	378.1	n.d.	0.28	1.74
1	75	60	5.962	34.3	17.8	277.3	0.06	0.22	1.25
2	75	228	5.783	34.5	17.6	286.6	0.33	0.30	0.97
3	75	300	5.947	34.2	17.5	278.4	n.d.	0.27	0.95
4	75	396	6.002	40.8	21.4	348.1	n.d.	0.32	0.90
AO-3	Temp. (°C)	Time (hr)	pH_{25C}	[a]Σ[Mg]	Σ[Ca]	[b]Σ[SiO_2]	Σ[Fe]	Σ[P]	$(^{29}Si/^{28}Si)_{Aq}$
0	50	12	5.248	56.0	12.7	510.5	0.12	0.38	0.05
1	50	132	5.421	48.3	11.0	730.4	0.55	0.55	0.05
2	50	204	5.767	58.7	13.7	1022.1	4.65	1.19	0.05
3	50	300	5.252	62.6	14.7	1244.2	10.42	2.26	0.05
AO-4	Temp. (°C)	Time (hr)	pH_{25C}	[a]Σ[Mg]	Σ[Ca]	[b]Σ[SiO_2]	Σ[Fe]	Σ[P]	$(^{29}Si/^{28}Si)_{Aq}$
0	50	12	4.562	61.6	13.6	134.4	4.04	0.16	0.04
1	50	132	4.609	44.3	9.9	169.0	5.07	0.19	0.04
2	50	204	4.753	65.1	14.4	292.4	5.73	0.12	0.04
3	50	300	5.246	55.8	12.6	266.3	2.48	0.13	0.04

[a]The major dissolved cations/anions are in units of mmol/kg. [b]The minor dissolved cations/anions are in units of umol/kg. All of the experiments used natural reactant basalt that was treated with the CBD treatment, a reductive dissolution pretreatment to specifically remove any pre-existing Fe^{3+}-oxide minerals associated with the natural basalt recovered from the seafloor.

4.2.2. $^{29}Si/^{28}Si$

As explained by Equation 1, in experiments with a $^{29}SiO_2$ spike, a decrease in the $^{29}Si/^{28}Si$ ratio is representative of reaction progress due to the dissolution of reactant basalt and the associated mixing of isotopically natural SiO_2. The initial $^{29}Si/^{28}Si$ ratio of SW-1, used in oxygenated experiments PG-1, PG-2, and PG-3, was 0.30. The initial $^{29}Si/^{28}Si$ ratio of SW-4, used in anoxic experiments AO-1 and AO-2, was 9.64. In the two anoxic experiments with a $^{29}SiO_2$ spike, the $^{29}Si/^{28}Si$ ratio decreased significantly over the 396-hour course of the experiments (Table 5; Fig. 2a). The initial samples taken at 12 hours had $^{29}Si/^{28}Si$ ratios of 0.63 and 1.74, respectively, indicating a rapid onset of dissolution. By the final sample, these ratios had decreased to 0.14 and 0.90, respectively. The $^{29}Si/^{28}Si$ ratio of the three oxygenated experiments with a $^{29}SiO_2$ spike, on the other hand, stayed constant at 0.30 throughout the course of the experiments (Table 4; Fig. 3a)

Figure 1: AO-3 time-series solution chemistry

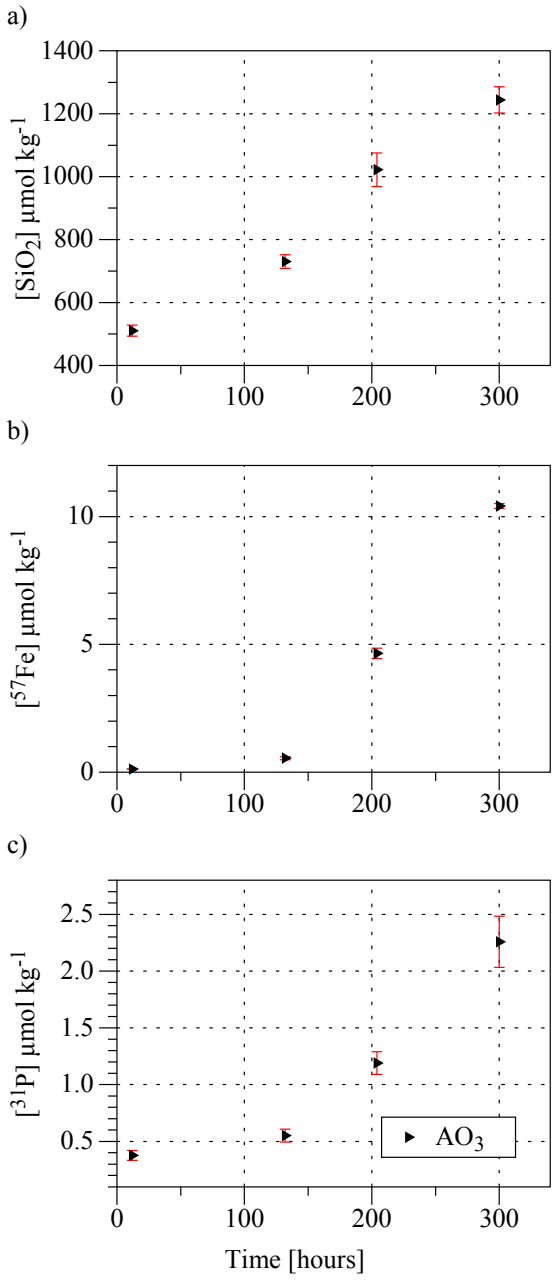

Fig. 1: Time-series solution chemistry of synthetic seawater upon reaction with basalt glass under anoxic conditions in experiment AO-3, which did not have an initial spike of $^{29}SiO_2$. **(a)** Reaction progress is thus demonstrated by an increase in total SiO_2 concentration. **(b, c)** With reaction progress, concentrations of both ^{31}P and ^{57}Fe increase, which is indicative of a liberation of PO_4^{3-} derived from basalt into solution with negligible Fe^{3+}-oxide mineral formation.

4.2.3. Dissolved phosphorus (P)

It is expected that in anoxic conditions, which inhibit the oxidation of Fe^{2+} to Fe^{3+} and thus the adsorption of phosphorus onto secondary Fe^{3+}-oxide is limited, dissolution of reactant basalt would be associated with an increase in dissolved phosphorus concentrations. In the two anoxic experiments conducted at 75 ˚C, dissolved P concentrations increased significantly: from 0.26 to 1.18 µmol kg^{-1} in AO-1 and from 0.38 to 2.26 µmol kg^{-1} in AO-3 (Fig. 2c, Fig. 1c, Table 5). Anoxic experiments at 50 ˚C, AO-2 and AO-4, did not have a significant increase in dissolved phosphorus concentrations, with levels staying below 0.32 and 0.19 µmol kg^{-1} respectively (Fig. 2c; Table 5).

Conversely, phosphorus liberation is expected to be limited in oxygenated experiments due to P adsorption onto secondary Fe^{3+}-oxide minerals. None of the oxygenated experiments had an increase in dissolved phosphorus concentrations, and the one oxygenated experiment that was initiated with initially elevated PO_4^{3-} levels (PG-3) saw a decrease in dissolved phosphorus concentrations from 45.05 to 42.08 µmol kg^{-1} (Table 4).

Figure 2: AO-1, 2 time-series solution chemistry

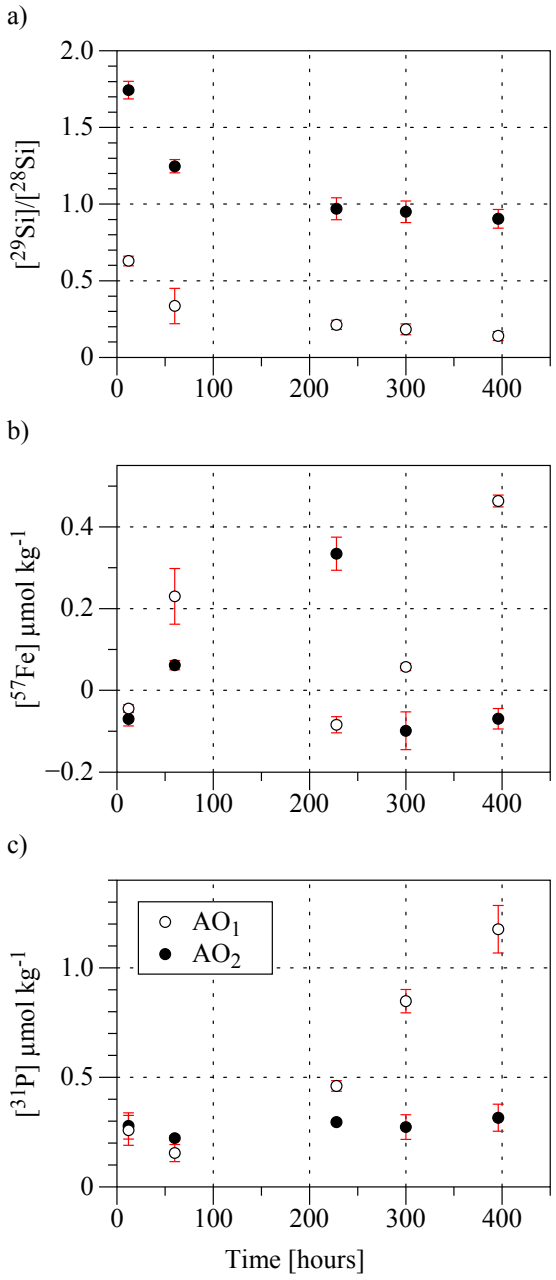

Fig. 2: Time-series solution chemistry of synthetic seawater upon reaction with basalt glass under anoxic conditions in experiments AO-1 and AO-2. **(a)** AO-1 and AO-2 utilized a $^{29}SiO_2$ isotope spike and had an initial solution $^{29}Si/^{28}Si$ ratio of 9.64. Reaction progress is demonstrated by a decrease in the $^{29}Si/^{28}Si$ ratio. **(b)** The constant low ^{57}Fe concentrations could be the result of Fe_2SiO_4 precipitation due to high SiO_2 concentrations. **(c)** With reaction progress, concentrations of ^{31}P increase, which is indicative of a release of PO_4^{3-} derived from basalt into solution in the absence of Fe^{3+}-oxides.

4.2.4. Dissolved iron (Fe)

It is expected that in anoxic conditions, dissolution of reactant basalt would be associated with an increase in dissolved Fe concentrations. In experiment AO-3, dissolved Fe concentrations increased dramatically from 0.12 to 10.42 µmol kg^{-1} (Fig. 1b; Table 5). Concentrations did not increase as linearly or dramatically in experiment AO-4; after an initial increase from 4.04 µmol kg^{-1} to 5.73 µmol kg^{-1}, they dropped to 2.48 µmol kg^{-1} in the final sample (Table 5). Even this final concentration, however, represents a significant increase in dissolved Fe concentration compared to the synthetic seawater solution concentration of 0 µmol kg^{-1}. Both anoxic experiments conducted with an initial $^{29}SiO_2$ spike did not have a significant increase in dissolved Fe concentrations, with levels staying near or below detection limits (Fig. 2b; Table 5). Conversely, Fe liberation is expected to be limited in oxygenated experiments due to the formation of secondary Fe^{3+}-oxide minerals. None of the oxygenated experiments had an increase in dissolved Fe concentrations (Table 4).

4.3. Scanning electron microscopy

Altered basalt glass powder from experiments AO-1 and PG-3 were observed by SEM and compared to unaltered reactant basalt

Figure 3: PG-1, 2 time-series solution chemistry

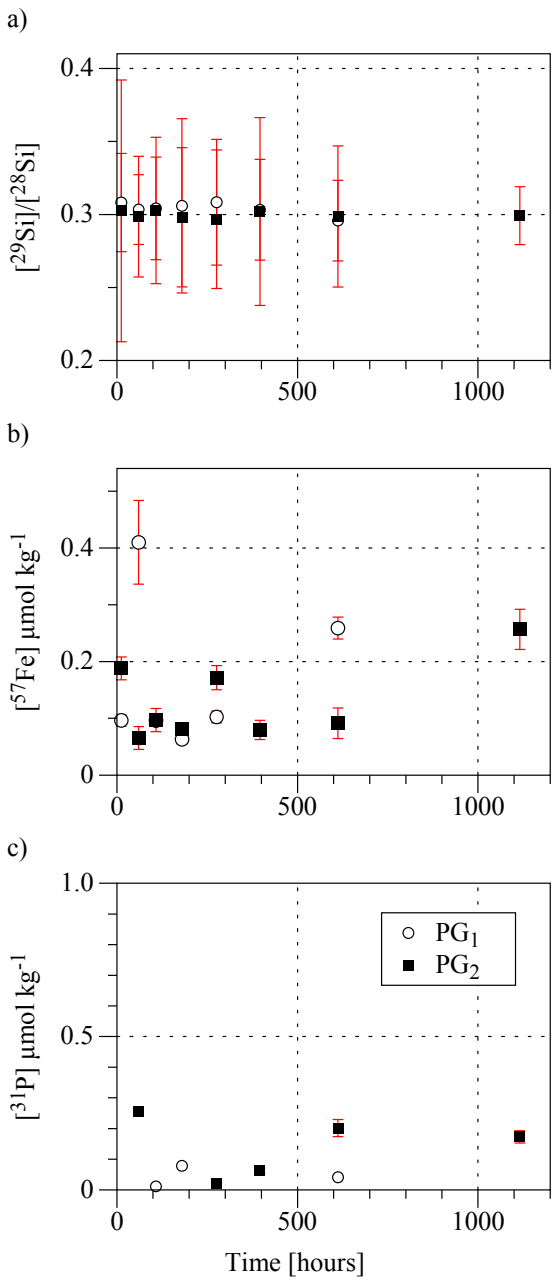

Fig. 3: Time-series solution chemistry plots for experiments PG-1 and PG-2, which utilized a $^{29}SiO_2$ isotope spike and had an initial solution $^{29}Si/^{28}Si$ ratio 0.30. **(a)** Reaction progress is demonstrated by a decrease in the $^{29}Si/^{28}Si$ ratio. **(b,c)** Consistent low concentrations of ^{31}P and ^{57}Fe are indicative of PO_4^{3-} release being inhibited by adsorption onto Fe^{3+}-oxides. Measured [^{31}P] values below zero are excluded.

glass powder that had been treated with CDB to remove pre-existing secondary Fe^{3+}-oxide minerals (Fig. 4). Average grain size was approximately 5-50 µm (Fig. 4a). The fresh basalt powder (Fig. 4a) had a smooth surface with no evidence of alteration. This is in stark contrast with the basalt glass powder altered in experiment AO-1 (anoxic conditions at 75 °C), which exhibits extensive alteration with the formation of an layer of clay secondary minerals on the surface of powder grains (Fig. 4b). Basalt glass powder from the lower temperature (5 °C) oxgenated experiment PG-1 (Fig. 4c) does not exhibit extensive clay mineral formation, but the surface does appear to be slightly alterered, with cleavage planes less well defined than in the unaltered basalt glass sample.

4.4. Synchrotron X-ray fluorescence mapping (SXRF)

Images of the reactant powdered basalt produced by SXRF (Fig. 5) demonstrate that both the glass fraction and the crystalline fraction of the are nearly chemically homogenous. This makes the powdered basalt glass an ideal reactant as the flux of dissolution products will be spatially consistent throughout the powder and within individual grains.

5. Discussion

Figure 4: SEM images of powdered reactant basalt glass before and after alteration.

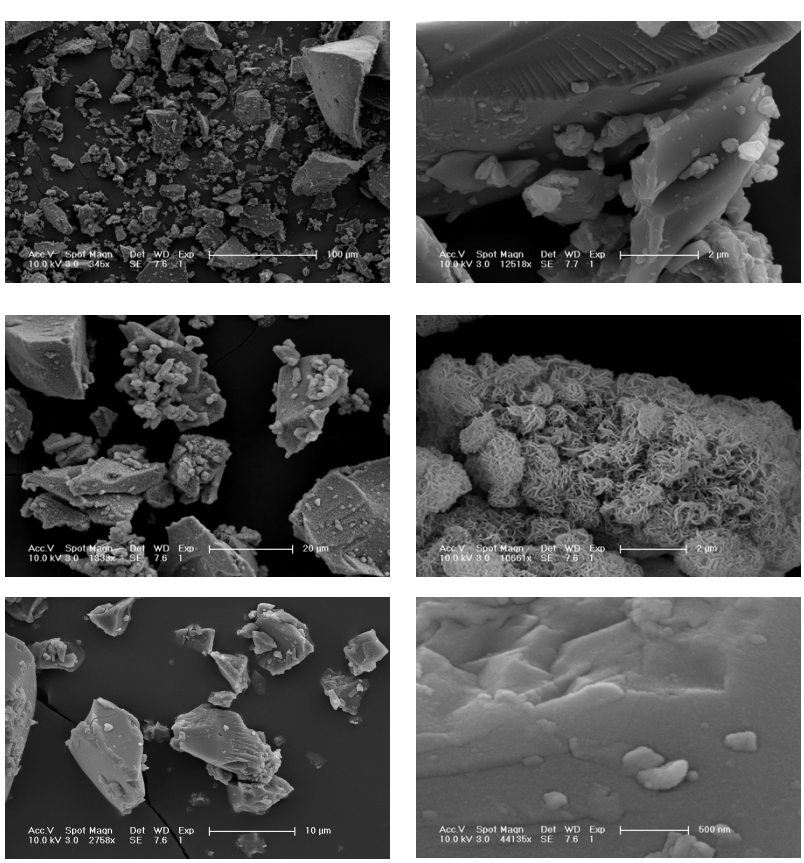

a) Non-experimentally altered reactant powdered basalt glass. **b)** Powdered basalt glass after alteration in anoxic conditions at 75 °C in experiment AO-1. **c)** Powdered basalt glass after alteration at present oxygen levels at 5 °C in experiment PG-3.

The results from our oxygenated experiments and our anoxic experiments are in support of a framework in which anoxic weathering of oceanic crust can be a significant source of phosphorus to the oceans. This is demonstrated most clearly in the results from experiment AO-3 (Fig. 1), but is also indicated by the results from experiment AO-1 (Fig. 2). Both were conducted at in anoxic conditions at 75 °C, the highest reaction temperature included in our set of experiments. This elevated temperature, which is moderate within the context of hydrothermal ridge-flank vent systesm, allowed the reaction to proceed quickly enough to have a significant change in reaction fluid composition within the experimental timeframe. The systematic decrease in $^{29}Si/^{28}Si$ ratio with time in AO-1 is reflective of basalt dissolution, which dilutes the initial $^{29}SiO_2$ spike through mixing with isotopically natural basalt derived SiO_2. Because experiment AO-3 did not utilize a $^{29}SiO_2$ spike, reaction progress is instead visualized by a systematic increase in total SiO_2 concentrations which is also indicative of basalt derived SiO_2 rapidly going into solution; even just within the 12 hours before the first sample, concentrations increased from 0 to 510.5 μmol kg^{-1}. That both reactions demonstrated a significant increase in fluid phosphorus concentration is significant, and is in stark contrast to the prevailing model wherin phosphorus is assumed to not be derived from

MORB alteration. The simultaneous increase in dissolved Fe in AO-3 supports the hypothesis that the liberation of phosphorus to solution in anoxic conditions is possible due to the absence of Fe^{3+}-oxides; this secondary mineral formation would preclude an increase in solution Fe concentration because any Fe^{2+} liberated in basalt dissolution would be sequstered in alteration products.

It is notable, then, that experiment AO-1 did not also have an increase in dissolved Fe concentration associated with the increase in dissolved phosphorus. Instead, Fe concentrations remained below 0.5 µmol kg^{-1} for the duration of the experiment. The only significant difference between the two experiments was the initial 100 µmol kg^{-1} $^{29}SiO_2$ spike added to the synthetic seawater reaction solution in AO-1. Given that both the decrease in $^{29}Si/^{28}Si$ ratio and the increase in phosphorus concentration are in line with experiment AO-3 and with the framework of phosphorus liberation in the absence of Fe^{3+}-oxides, the consistently low Fe concentration in AO-1 might be the result of inhibitory behavior by the SiO_2 saturated reaction solution. The same Fe behavior is observed in AO-2, which also had an initial 100 µmol kg^{-1} $^{29}SiO_2$ spike concentration and a decrease in the $^{29}Si/^{28}Si$ ratio with time indicating basalt dissolution.

SiO_2 solution saturation has been experimentally shown to – in long-term, moderate-temperature, oxygenated conditions – lead to synthetic basalt glass alteration characterized by the formation of an amorphous silica layer and a clay layer enriched in Mg, Al, K, Ti, Mn, Fe and Ni (Ducasse et al., 2018). While these alteration experiments had a much higher solution concentration of $^{29}SiO_2$ at 160 mg kg^{-1}, the mechanism could still apply. Importantly, these alteration experiments did not result in a reaction rate limiting

Figure 5: SXRF images of reactant basalt

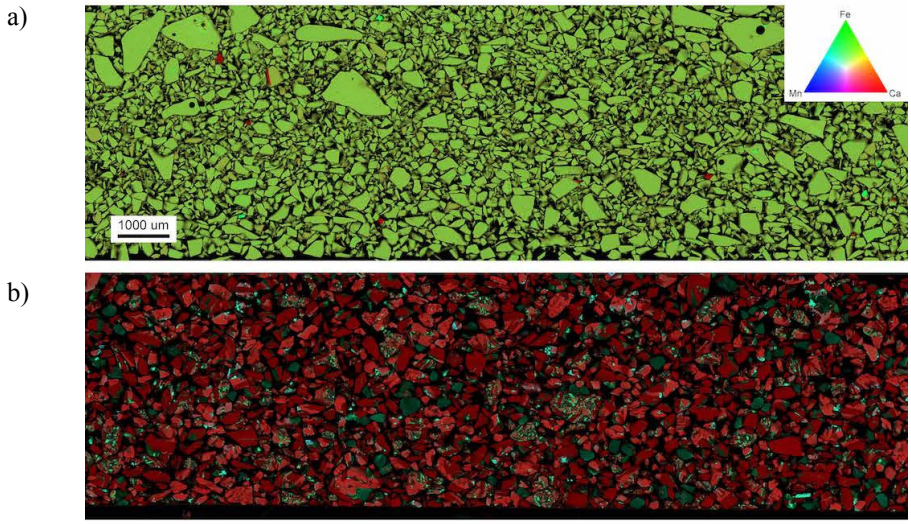

a) SXRF map of glass fraction and the **b)** crystalline fraction of reactant basalt isolated from near the axis of Juan de Fuca Ridge.

passivating layer on synthetic basalt glass grains. The effect on phosphorus concentrations was not reported. This proposed explanation for the inhibition of Fe release into solution in AO-1 and AO-2 is supported by SEM images of the altered basalt grains (Fig. 4), which provide visual confirmation of clay formation on the surface of the glass.

Oxygenated experiments, which were conducted at lower temperatures, did not exhibit significant changes in P or Fe concentrations with time. This is likely a function of both the lower reaction temperatures causing limited basalt dissolution and the fact that any released Fe from dissolution would quickly form Fe^{3+}-oxides, which would in turn adsorb any phosphorus released to solution. The prediction that basalt alteration was limited is corroborated by SEM imaging of PG-1 which does not show any extensive clay mineral formation like was found on AO-1. The surface does appear to be slightly alterered, however, with cleavage planes less well defined than in the unaltered basalt glass sample. Slight alteration of anoxic reactant basalt is in line with the slight increase in total dissolved SiO_2 exhibited in PG-4. The larger increase in total dissolved SiO_2 exhibited in PG-5 is likely due to its slightly higher 25 °C reaction temperature. Experiment PG-3 was initiated with an elevated PO_4^{3-} concentration, which went down slightly over time. This is likely indicative of limited adsorption of dissolved P onto Fe^{3+}-oxides.

Overall, the time-series solution chemistry of the anoxic basalt glass alteration experiments are in strong support of a submarine weathering framework wherein the absence of secondary Fe^{3+}-oxide minerals allows for the liberation of dissolved P to seawater.

6. Summary

Our results stand in strong contrast to the prevailing conceptual model wherein submarine weathering of oceanic crust is precluded from being a source of phosphorus to the oceans due to the presence of secondary Fe^{3+}-oxide minerals, and thus provide impetus to revisit mechanistic models for Earth's earliest oxygen cycle and the factors regulating the oxygen cycles of volatile-rich silicate planets more generally. Moving forward, it will be important to establish the ocean-atmosphere O_2 'threshold' above which oxygenation of the deep oceans attenuates bioavailable P fluxes by initiating widespread Fe^{2+} oxidation within the ocean interior. Intriguingly, existing model results indicate the possibility that atmospheric O_2 could be present at abundances that would potentially be remotely detectable without fully ventilating the deep oceans (Ozaki et al.,

2019; Christopher T. Reinhard et al., 2017; C. T. Reinhard et al., 2017), with the implication that terrestrial planets with water inventories similar to but greater than that of Earth could be very promising targets in the search for exoplanet biosignatures. Our experimental results provide strong evidence that fluxes of bioavailable P on terrestrial planets dominated by submarine basalt weathering under anoxic conditions — including the Hadean/Eoarchean Earth — are likely to be very robust and in some cases may surpass those of even the modern Earth system. Anoxic submarine weathering should thus be considered an important component of the large-scale redox balance of terrestrial planets.

Acknowledgements

There are several people without whom this project would not have succeeded. I owe endless thanks to Noah Planavsky, whose guidance, direction, aid, and encouragement not only on this thesis but in my desire to continue studying geochemistry has sustained my conviction in the face of self-doubt. Thank you for your investment in me, and for pushing me to push myself.

No part of this project would have been possible without Drew Syverson, a mentor and friend. Thank you for trusting me with your project, for the tremendous amount of support not only in our experiments but also in my learning to navigate the world of geology, and for indulging me in talking shop about bikes.

Lastly, I owe a debt of gratitude to my family and friends for listening when I gush about space and rocks, and for sharing their passions with me, too.

References

Berner, R. A. (1973). Phosphate removal from sea water by adsorption on volcanogenic ferric oxides. *Earth and Planetary Science Letters, 18*(1), 77-86. http://www.sciencedirect.com/science/article/pii/0012821X7390037X

Bjerrum, C. J., & Canfield, D. E. (2002). Ocean productivity before about 1.9 Gyr ago limited by phosphorus adsorption onto iron oxides. *Nature, 417*(6885), 159-162. https://doi.org/10.1038/417159a

Cockell, C. S., Bush, T., Bryce, C., Direito, S., Fox-Powell, M., Harrison, J. P., et al. (2016). Habitability: A Review. *Astrobiology, 16*(1), 89-117. https://doi.org/10.1089/ast.2015.1295

Coogan, L. A., & Gillis, K. M. (2013). Evidence that low-temperature oceanic hydrothermal systems play an important role in the silicate-carbonate weathering cycle and long-term climate regulation. *Geochemistry, Geophysics, Geosystems, 14*(6), 1771-1786.

Cox, G. M., Lyons, T. W., Mitchell, R. N., Hasterok, D., & Gard, M. (2018). Linking the rise of atmospheric oxygen to growth in the continental phosphorus inventory. *Earth and Planetary Science Letters, 489*, 28-36.

Ducasse, T., Gourgiotis, A., Pringle, E., Moynier, F., Frugier, P., Jollivet, P., & Gin, S. (2018). Alteration of synthetic basaltic glass in silica saturated conditions: Analogy with nuclear glass. *Applied Geochemistry, 97*, 19-31.

Fisher, L. A., Fougerouse, D., Cleverley, J. S., Ryan, C. G., Micklethwaite, S., Halfpenny, A., et al. (2015). Quantified, multi-scale X-ray fluorescence element mapping using the Maia detector array: application to mineral deposit studies. *Mineralium Deposita, 50*(6), 665-674. journal article. https://doi.org/10.1007/s00126-014-0562-z

Haymon, R. M., Fornari, D. J., Edwards, M. H., Carbotte, S., Wright, D., & Macdonald, K. C. (1991). Hydrothermal vent distribution along the East Pacific Rise crest (9°09′–54′N) and its relationship to magmatic and tectonic processes on fast-spreading mid-ocean ridges. *Earth and Planetary Science Letters, 104*(2), 513-534. http://www.sciencedirect.com/science/article/pii/0012821X91902268

Koritnig, S. (1965). Geochemistry of phosphorus—I. The replacement of Si4+ by P5+ in rock-forming silicate minerals. *Geochimica et Cosmochimica Acta, 29*(5), 361-371. http://www.sciencedirect.com/science/article/pii/0016703765900335

Laakso, T. A., & Schrag, D. P. (2014). Regulation of atmospheric oxygen during the Proterozoic. *Earth and Planetary Science Letters, 388*, 81-91.

Laakso, T. A., & Schrag, D. P. (2018). Limitations on Limitation. *Global Biogeochemical Cycles, 32*(3), 486-496.

Lingam, M., & Loeb, A. (2018). Is Extraterrestrial Life Suppressed on Subsurface Ocean Worlds due to the Paucity of Bioessential Elements? *The Astronomical Journal, 156*(4).

Lingam, M., & Loeb, A. (2019). Dependence of Biological Activity on the Surface Water Fraction of Planets. *The Astronomical Journal, 157*(1).

Mehra, O. P., & Jackson, M. L. (1958). Iron oxide removal from soils and clays by a dithionite-citrate system buffered with sodium bicarbonate. *Clays and Clay Minerals, 7*(1), 317-327.

Mills, B., Lenton, T. M., & Watson, A. J. (2014). Proterozoic oxygen rise linked to shifting balance between seafloor and terrestrial weathering. *Proc Natl Acad Sci U S A, 111*(25), 9073-9078. https://www.ncbi.nlm.nih.gov/pubmed/24927553

Och, L. M., & Shields-Zhou, G. A. (2012). The Neoproterozoic oxygenation event: Environmental perturbations and biogeochemical cycling. *Earth-Science Reviews, 110*(1-4), 26-57.

Ozaki, K., Reinhard, C. T., & Tajika, E. (2019). A sluggish mid-Proterozoic biosphere and its effect on Earth's redox balance. *Geobiology, 17*(1), 3-11. https://onlinelibrary.wiley.com/doi/abs/10.1111/gbi.12317

Poulton, S. W., & Canfield, D. E. (2011). Ferruginous Conditions: A Dominant Feature of the Ocean through Earth's History. *Elements, 7*(2), 107-112.

Reinhard, C. T., Olson, S. L., Schwieterman, E. W., & Lyons, T. W. (2017). False Negatives for Remote Life Detection on Ocean-Bearing Planets: Lessons from the Early Earth. *Astrobiology, 17*(4), 287-297. https://doi.org/10.1089/ast.2016.1598

Reinhard, C. T., Planavsky, N. J., Gill, B. C., Ozaki, K., Robbins, L. J., Lyons, T. W., et al. (2017). Evolution of the global phosphorus cycle. *Nature, 541*(7637), 386-389. https://www.ncbi.nlm.nih.gov/pubmed/28002400

Rouxel, O., Toner, B. M., Manganini, S. J., & German, C. R. (2016). Geochemistry and iron isotope systematics of hydrothermal plume fall-out at East Pacific Rise 9°50′N. *Chemical Geology, 441*, 212-234.

Ruttenberg, K. C. (2003). 8.13 - The Global Phosphorus Cycle. In H. D. Holland & K. K. Turekian (Eds.), *Treatise on Geochemistry* (pp. 585-643). Oxford: Pergamon.

Ruttenberg, K. C., & Sulak, D. J. (2011). Sorption and desorption of dissolved organic phosphorus onto iron (oxyhydr)oxides in seawater. *Geochimica et Cosmochimica Acta, 75*(15), 4095-4112.

Simpson, F. (2017). Bayesian evidence for the prevalence of waterworlds. *Monthly Notices of the Royal Astronomical Society, 468*(3), 2803-2815. https://doi.org/10.1093/mnras/stx516

Staudigel, H. (2003). 3.15 - Hydrothermal Alteration Processes in the Oceanic Crust. In H. D. Holland & K. K. Turekian (Eds.), *Treatise on Geochemistry* (pp. 511-535). Oxford: Pergamon.

Stein, C. A., & Stein, S. (1994). Constraints on hydrothermal heat flux through the oceanic lithosphere from global heat flow. *Journal of Geophysical Research: Solid Earth, 99*(B2), 3081-3095. https://agupubs.onlinelibrary.wiley.com/doi/abs/10.1029/93JB02222

Trocine, R. P., & Trefry, J. H. (1988). Distribution and chemistry of suspended particles from an active hydrothermal vent site on the Mid-Atlantic Ridge at 26°N. *Earth and Planetary Science Letters, 88*(1), 1-15. http://www.sciencedirect.com/science/article/pii/0012821X88900416

Tyrrell, T. (1999). The relative influences of nitrogen and phosphorus on oceanic primary production. *Nature, 400*(6744), 525-531. https://doi.org/10.1038/22941

Watson, E. B. (1980). Apatite and phosphorus in mantle source regions: An experimental study of apatite/melt equilibria at pressures to 25 kbar. *Earth and Planetary Science Letters, 51*(2), 322-335.

Wheat, C. G., Feely, R. A., & Mottl, M. J. (1996). Phosphate removal by oceanic hydrothermal processes: An update of the phosphorus budget in the oceans. *Geochimica et Cosmochimica Acta, 60*(19), 3593-3608. http://www.sciencedirect.com/science/article/pii/0016703796001895

Wheat, C. G., Fisher, A. T., McManus, J., Hulme, S. M., & Orcutt, B. N. (2017). Cool seafloor hydrothermal springs reveal global geochemical fluxes. *Earth and Planetary Science Letters, 476*, 179-188.

Wheat, C. G., & Mottl, M. J. (2000). Composition of pore and spring waters from Baby Bare: global implications of geochemical fluxes from a ridge flank hydrothermal system. *Geochimica et Cosmochimica Acta, 64*(4), 629-642. http://www.sciencedirect.com/science/article/pii/S0016703799003476

Zhu, C., Liu, Z., Schaefer, A., Wang, C., Zhang, G., Gruber, C., et al. (2014). Silicon Isotopes as a New Method of Measuring Silicate Mineral Reaction Rates at Ambient Temperature. *Procedia Earth and Planetary Science, 10*, 189-193.

Zhu, C., Liu, Z., Zhang, Y., Wang, C., Scheafer, A., Lu, P., et al. (2016). Measuring silicate mineral dissolution rates using Si isotope doping. *Chemical Geology, 445*, 146-163.